Journal of Membrane Science 511 (2016) 108–118

Contents lists available at ScienceDirect

Journal of Membrane Science

journal homepage: www.elsevier.com/locate/memsci

Designing asymmetric multilayered membrane filters with improved performance

I.M. Griffiths [a,*], A. Kumar [b], P.S. Stewart [c]

[a] Mathematical Institute, Radcliffe Observatory Quarter, Oxford, OX2 6GG, UK
[b] Pall Life Sciences, 20 Walkup Drive, Westborough, MA 01581, USA
[c] School of Mathematics and Statistics, University of Glasgow, G12 8QW, UK

ARTICLE INFO

Article history:
Received 28 October 2015
Received in revised form
8 February 2016
Accepted 11 February 2016
Available online 25 March 2016

Keywords:
Filtration
Multilayer membranes
Fouling
Pore clogging
Network model
Mathematical modelling

ABSTRACT

Asymmetric multilayered filters, comprising a series of membranes with varying pore sizes stacked on top of one another, allow filtration to be tailored in a variety of novel ways. We develop a network model that systematically captures the complex filtration behaviour in such multilayer filters. The model allows us to understand the response of the system when challenged with a particular feed composition, characterized through the particle size and adhesivity to the membrane. We show how the model enables comprehensive and time-efficient sweeps in parameter space to be conducted that determine the optimal multilayered filter configuration for a given filtration challenge, classified by the number of membrane layers, the change in pore size between each layer (filter taper angle), and the level of transpore interconnectivity between each layer. The model allows us to isolate and analyse the effect of each of the specific filter characteristics and identify the practical merits and disadvantages. In particular, we predict that the optimal arrangement for maximizing throughput through the filter is to have pore radius gradually decreasing with depth, and a slight level of pore interconnectivity, with the precise set-up a function of the particle size, adhesivity and number of filter layers. The results of the analysis are used to draw conclusions on the design of membrane filters for optimal filter performance.

1. Introduction

Membrane filtration can be tailored in a variety of ways by using a multilayered structure, composed of an array of membranes with different pore sizes stacked on one another. Such filters can, for example, offer a simple way of sequentially separating cells or particles [1,2], or combined to form the filtration support layers required in ultrafiltration, gas separation and catalysis [1]. In other cases, by using a membrane impregnated with bacteria-destroying medication in parallel with another that sieves particles, a greater spectrum of contaminants may be removed in one filtration process [3].

Filters whose porosity decreases with depth, or *porosity-graded asymmetric membranes* have been observed to improve efficiency [4–8]. Their increased efficiency can be qualitatively attributed to a decrease in porosity compensating for a reduction of contaminant concentration with depth, owing to prior filtering. This effect is particularly desirable, since often only a small portion of the filter media near the surface is actually involved in the active removal of contaminants, with much of the deeper filter media left unused when the filter clogs. This leads to premature clogging and thus inefficient use of the filter [9].

Despite the significant merits of multilayer filters being well-known in industry, a systematic study of the underlying mechanisms responsible for the superior performance that characterizes the internal behaviour of such multilayer filters during operation has yet to be explored. Currently, experimentally it is difficult to observe the internal particle trapping within a filter during the filtration process directly, with limited techniques only now beginning to emerge, such as positron annihilation spectroscopy [10,11]. Instead, deductions are made only after dissecting the porous medium once filtration has ceased. For these reasons, predicting and designing the optimal multilayer filter structure via a systematic series of experiments is impractical, and a theoretical study is highly desired.

Mathematical and computational methods allow for investigation of filtration challenges. Computational fluid dynamics (CFD) for modelling filtration scenarios are described in [12]. In the same paper, the authors use scanning electron microscopy to obtain a full description of a given membrane microstructure, and implement a full CFD model of particles moving within the

* Corresponding author.
E-mail address: ian.griffiths@maths.ox.ac.uk (I.M. Griffiths).

http://dx.doi.org/10.1016/j.memsci.2016.02.028
0376-7388/

membrane. While a full CFD simulation provides excellent insight into how an individual particle is trapped, computational costs associated with keeping track of all the particles within a complicated pore structure makes it impractical on a large scale.

Dalwadi et al. [13] use homogenization theory to explore the improved filtration observed in a continuous porosity-graded filter. The model presented describes the motion of contaminants within a continuous media as they are transported via advection and diffusion. The results corroborate experimental observations, and are able to predict the performance of a filter through a reduced and computationally efficient mathematical model. The model enables large-scale parameter sweeps to explore filtration behaviour, and assist in the selection of porosity-graded filters for a given challenge feed solution. The model, however, is limited in that it does not include filter blocking mechanisms.

In our previous study [14], a network model was laid out that captures blocking in a filter composed of discrete pores through the adhesion of particles to the internal pore structures (standard blocking), the complete blocking of pores, and formation of a cake layer on the surface of the membrane [15]. In particular, an emphasis was placed on a systematic method of coupling the interplay between each of these fouling routes. The model is able to demonstrate how an understanding of this coupling was essential to explain a series of recent experimental observations. As a consequence, the model is able to predict the type of fouling behaviour that is occurring at a given time by simply studying measurements of the volumetric flux and total throughput through the membrane, without the need for dissecting the filter.

In this paper we analyse the efficiency of a multilayer filter, composed of a series of membranes with varying pore sizes. We derive a network model, which develops the model laid out in [14], to simulate the transport of particles through a multilayer filter and the trapping within. The model allows for adhesion of particles that are able to pass within the membrane to the walls of the pores, and for complete blocking of pores for which the particles are too large to enter. Pore interconnectivity is also included, allowing particles that are not trapped within one layer to pass into a choice of pores in the next filter layer. The network model provides a predictive tool for choosing the appropriate membrane to use, characterized by taper angle, affinity of the membrane material to the particles, number of filter layers and the pore connectivity, for a given feed solution.

2. Filter characterization

We consider a filter of depth $\hat{h}$ composed of a series of N membranes of equal thickness $(\hat{h}/N)$ stacked on top of one other. We label each membrane layer in succession, with layer k corresponding to the kth membrane that the challenge feed will encounter. We consider each membrane layer to be composed of a two-dimensional $m \times n$ array of regularly spaced uniform pores, of initial radii $\hat{R}_k$ within the kth layer, as illustrated in Fig. 1. Here we study regimes in which the difference in pore radius between any two successive membranes is constant, but may reduce (a constricting filter) or increase (a dilating filter). We characterize this variation through the taper angle, α, defined by

$$\tan(\alpha) = \frac{\hat{R}_1 - \hat{R}_N}{\hat{h}}. \tag{1}$$

To enable comparison between different filters we consider setups in which the initial mean pore radius across the entire filter, $\langle \hat{R} \rangle$, is a constant, where

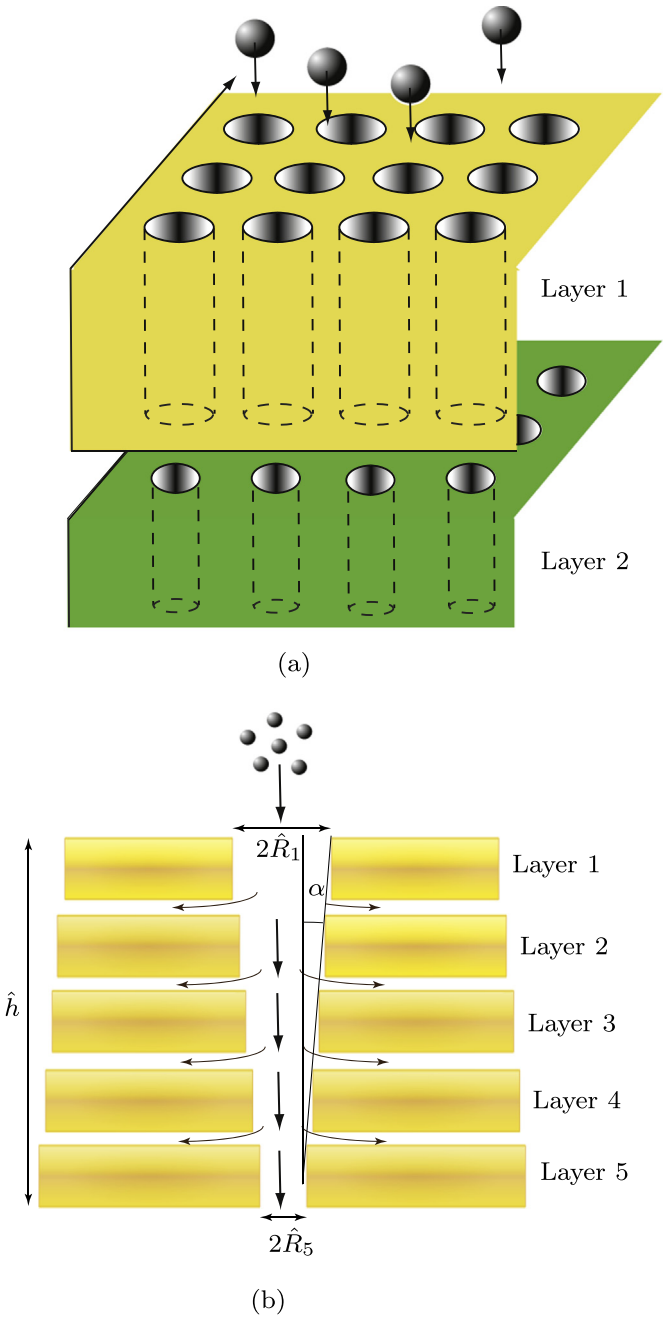

Fig. 1. (a) Schematic diagram of a multilayer filter. Each layer, k, is initially composed of an array of $n \times m$ equal-sized pores, but whose radius $\hat{R}_k$ may vary for each layer. (b) Front schematic view illustrating the different pore radii at each layer and the taper angle. At each level the particle may pass into the pore directly beneath, or may traverse to one of four neighbouring pores. (Here two neighbouring pores are shown; the additional two pores are located into and out of the page.) The total filter thickness is $\hat{h}$.

$$\langle \hat{R} \rangle = \frac{1}{N} \sum_{k=1}^{N} \hat{R}_k. \tag{2}$$

We also classify a membrane through the interconnectivity of pores between layers. Here we consider filters for which if a particle passes through a pore then it has the opportunity either to pass into the pore in the layer directly beneath or to traverse to one of the four neighbouring pores on the square grid (Fig. 1b). We denote the hydraulic conductivity of the connection to an adjacent pore by $\hat{\gamma}$: when $\hat{\gamma} = 0$ the particle passes directly to the next pore in the layer beneath and we call this a *non-connected filter*; when

$\hat{\gamma} \neq 0$ we have a *locally connected filter* and the particle may traverse to an adjacent pore instead of entering the pore directly beneath. The particle is then either able to enter this new pore or to traverse to a neighbour of this new pore site. We use a weighted probability for the pore selection based on the fluxes through the pores that favours pores through which there is a higher flux. When $\hat{\gamma} \to \infty$ the filter approaches *global connectivity*. In this limiting case the connections between pores offer no resistance and the particle enters the pore based solely on the relative pore fluxes and not the pore proximity.

3. Mathematical model

We apply a constant transmembrane pressure difference, $\Delta\hat{P}$, across the entire filter and examine the decline in volumetric flux, $\hat{Q}$, with increasing throughput, $\hat{V}$, defined by

$$\hat{V} = \int_0^{\hat{t}} \hat{Q}(s)\, \mathrm{d}s, \tag{3}$$

where $\hat{t}$ denotes time.

The flow rate through a given pore (i,j) in layer k at time $\hat{t}$, $\hat{q}_k^{(i,j)}(\hat{t})$, is given by Poiseuille's law [16],

$$\hat{q}_k^{(i,j)}(\hat{t}) = \frac{\pi N \Delta\hat{p}_k(t)\hat{r}_k^{(i,j)}(\hat{t})^4}{8\mu\hat{h}}, \tag{4}$$

where μ is the viscosity of the feed solution (assumed constant) and the pore radius $\hat{r}_k^{(i,j)}$ can change with time due to the fouling mechanisms. We note that $\hat{r}_k^{(i,j)}(0) = \hat{R}_k$, and recall that the depth of an individual membrane layer is $\hat{h}/N$. Unlike the single-layer model [14] we must also compute the pressure drop across each layer, $\Delta\hat{p}_k(t)$, $1 \le k \le N$. To achieve this we must determine the fluid pressure in the region between the membrane layers. For the region between layers k and $k+1$ at pore (i,j) we denote this pressure by $\hat{p}_{k+1/2}^{(i,j)}$ for $1 \le k \le N-1, 1 \le i \le m, 1 \le j \le n$. We set the outlet pressure to be zero without loss of generality, so then $p_{N+1/2}^{(i,j)} = 0$ and $p_{1/2}^{(i,j)} = \Delta P$. The pressure difference across pore k is then $\Delta\hat{p}_k^{(i,j)} = \hat{p}_{k-1/2}^{(i,j)} - \hat{p}_{k+1/2}^{(i,j)}$, for $1 \le k \le N$. The transverse flux between layers k and $k+1$ of pores (i,j) and $(i+1,j)$ in layer k is given by

$$\hat{q}_{k+1/2}^{(i,j)\to(i+1,j)} = \hat{\gamma}(\hat{p}_{k+1/2}^{(i,j)} - \hat{p}_{k+1/2}^{(i+1,j)}), \tag{5}$$

and similarly for the flux between other neighbouring pores.

In a similar manner to Kirchoff's law for an electrical circuit, we assume that the fluid flux entering each pore site is balanced by the flux leaving. At pore (i,j) between layers k and $k+1$ this implies that

$$\hat{q}_k^{(i,j)} = \hat{q}_{k+1}^{(i,j)} + \hat{q}_{k+1/2}^{(i,j)\to(i+1,j)} + \hat{q}_{k+1/2}^{(i,j)\to(i-1,j)} + \hat{q}_{k+1/2}^{(i,j)\to(i,j+1)} + \hat{q}_{k+1/2}^{(i,j)\to(i,j-1)}. \tag{6}$$

Since each flux depends linearly on the pressures $\hat{p}_{k+1/2}^{(i,j)}$ we can express the system as a matrix problem for $\hat{p}_{k+1/2}^{(i,j)}$, $1 \le k \le N-1$, $1 \le i \le m$, $1 \le j \le n$ which we solve numerically using MATLAB.

The total volumetric flow rate through each layer, $\hat{Q}_k$, is then given by the sum of the individual fluxes through all pores for that layer,

$$\hat{Q}_k = \sum_{i=1}^{m}\sum_{j=1}^{n} \hat{q}_k^{(i,j)}. \tag{7}$$

Conservation of mass ensures that, at any given time, $\hat{Q}_k$ must equal the flux through the entire filter, $\hat{Q}$, for all $1 \le k \le N$. The total volumetric throughput is given by

$$\hat{V} = \int_0^{\hat{t}} \hat{Q}(s)\, \mathrm{d}s. \tag{8}$$

The contaminants are assumed to be solid spherical particles of constant radius, $\hat{a}$. On average, a particle will arrive at the membrane every $1/\hat{C}\hat{Q}$ seconds, where $\hat{C}$ is the concentration (number of particles per unit volume). For any given experiment the particles will, in practice, arrive at times that are randomly distributed around this expected arrival value. However, we are concerned with the general fouling behaviour that is observed and so consider the result of the average of many numerical simulations. In doing so, any randomness in the particle arrival time that is observed for a single simulation will be smoothed out, and so it is sufficient for us to assume that particles arrive in a uniform manner with the fluid processed. All of the results presented in this paper are the average of 20 independent simulations for a grid size $m \times n = 7 \times 7$; the results yielded were found to be unchanged by increasing the number of independent simulations or grid size further.

To enable comparison between different model experiments, we scale the time and flux via

$$\hat{t} = \frac{t}{\hat{C}\hat{Q}(0)}, \quad \hat{Q}(\hat{t}) = \hat{Q}(0)Q(t), \tag{9}$$

so that, when $Q = 1$, a particle will arrive on average at the membrane every unit dimensionless time. The dimensionless throughput is then

$$V = \int_0^t Q(s)\, \mathrm{d}s. \tag{10}$$

We also scale all lengths with the mean pore radius,

$$\hat{r}_k^{(i,j)} = \langle\hat{R}\rangle r_k^{(i,j)}, \quad \hat{h} = \langle\hat{R}\rangle h, \quad \hat{a} = \langle\hat{R}\rangle a, \tag{11}$$

so the taper angle, α, is given by

$$\tan(\alpha) = \frac{R_N - R_1}{h}. \tag{12}$$

We define the relative hydraulic conductivity,

$$\gamma = \frac{8\hat{\gamma}\mu}{\pi\hat{R}^3}, \tag{13}$$

which compares the favourability of traversing to another pore compared with direct transmission to the pore beneath. For a membrane comprising uniformly spaced pores of equal pore radius, the probability of traversing to and then travelling through an adjacent pore compared with passing into the pore directly beneath is given by

$$\kappa = \frac{h/N}{\gamma + h/N}; \tag{14}$$

$\kappa(\le 1)$ gives a measure of the probability of a particle to progress directly into the pore below rather than traversing to a neighbouring pore before progressing to the next layer. For a membrane whose pore structure is anisotropic it is possible that particles may favour traversing to another pore over direct transmission to the layer beneath. (Such an effect has been observed with PVDF membranes by Ho and Zydney [17].)

As discussed above, the flux of fluid through each pore, and thus the fouling rate, is affected by various mechanisms. In the following section we detail the effect of each of these fouling

mechanisms and how they are accounted for within the network model.

4. Routes to membrane fouling

4.1. Standard blocking

We assume that all blocking is constrained to within the pores and not in the pore connections. If a particle of size a arrives at pore (i,j) in layer k and $a < r_k^{(i,j)}$ then the particle enters into the internal pore structure. Once within the pore we allow for a finite probability of particle adhesion to the pore wall, p_a. This probability will in practice be a complex function that depends on many features, such as membrane and contaminant composition and geometry. For simplicity, here we suppose that p_a is a constant for each layer, although the mathematical model readily generalizes to more complex adhesion laws (see, for example, [14]).

The radii of the pores will shrink in response to the internal deposition of particles and on average, for the simplest model for radial contraction, the pore radius following deposition of $n \geq 1$ particles will be $\sqrt{r_k^{(i,j)2} - 4na^3/3h}$, as illustrated in Fig. 2(a). Thus, the total number of particles that may be admitted by a pore in layer k before complete blocking occurs, T_k, is given by

$$T_k(a, h) = \text{Ceiling}\frac{3(R_k^2 - a^2)h}{4a^3}, \tag{15}$$

where Ceiling(x) denotes the ceiling function that returns the smallest integer not less than x. This mechanism of reduction in flux is termed *standard blocking*.

4.2. Complete blocking

If the particle of size a lands on an open pore (i,j) of size $r_k^{(i,j)}$ and $a > r_k^{(i,j)}$ then *complete pore blocking* occurs (Fig. 2). In practice this particle may create an imperfect seal around the pore, so that fluid continues to flow through the pore. However, the flux through a pore following complete blocking is typically much lower than the flux through an open pore, and so in general the filtration process no longer becomes practical following complete blocking and filtration ceases. As a result, we assume that a perfect seal is made when a particle completely blocks a pore without losing any of the features observed during a typical filtration run. (For more details on the implementation and a study of the effect of leakage due to an imperfectly sealed pore see [14].)

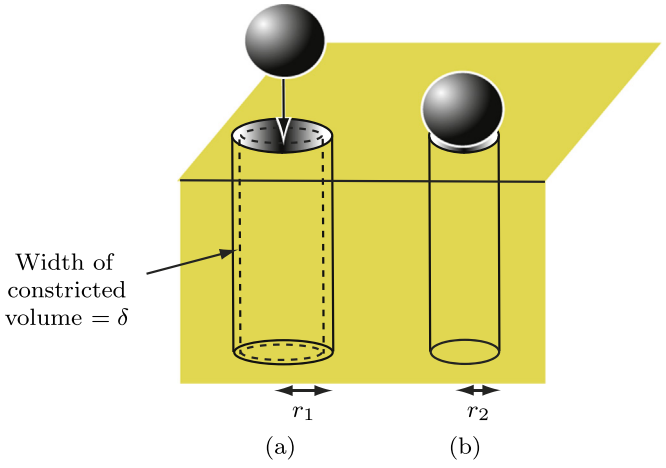

Fig. 2. Schematic diagram of possible blocking mechanisms: (a) *Standard blocking*: Here pore radius $r_1 > a$. Upon acceptance of $n \geq 1$ particles the pore radius reduces to a new radius $\sqrt{r_1^2 - 4na^3/3h}$. (b) *Complete blocking*: Here the pore radius $r_2 < a$.

In this paper the network model we derive is used as a framework to explore the impact that the filter properties, namely the taper angle, pore interconnectivity between the membrane layers, and number of layers, has on the filtration efficiency. The model will allow us to conduct extensive parameter sweeps that are impractical, or in some cases even impossible, to achieve experimentally. The resulting data will be used to make predictions on the strategy for optimal membrane selection based on a given feed composition, characterized through particle size and adhesivity to the membrane.

5. Influence of taper angle

5.1. An optimal taper angle

To examine the effect of taper angle on the filtration efficiency we first consider a non-connected filter ($\gamma = 0$), for which particles that exit a pore in a given layer transit to the pore directly beneath. We consider a set-up composed of five membrane layers ($N=5$) and vary the taper angle, α, defined by (12). As the taper angle increases the rate at which the flux declines with throughput is unchanged in the early stages, but a convex region appears in the QV signature for larger values of V (i.e., a region where $d^2Q/dV^2 > 0$), as seen in the dot-dashed line in Fig. 3. This arises due to the reduced flux decline, which ultimately leads to a higher total amount of fluid processed before clogging occurs, i.e., an increase in $V(t \to \infty)$, which we denote by V^*. However, we find that, as the taper angle increases further, V^* begins to fall again and the improvements in filtration efficiency are lost (Fig. 3, dotted line). Similarly, we find that filters with a negative taper angle yield a reduced total throughput, and exhibit an entirely concave downward QV signature, that is, one for which $d^2Q/dV^2 < 0$ everywhere (Fig. 3, solid line). The possibility of convex regions in the QV signature for some taper angles prohibits self-similar collapse when scaling the graphs with the final throughput.

The existence of an optimal taper angle that maximizes the throughput is clearly seen in Fig. 4, where a continuous dependence on taper angle is extracted. We may rationalize the observation of improved total throughput by examining the rate of pore constriction in each of the membrane layers. As contaminants enter the membrane they will adhere to the pore walls at a rate proportional to the contaminant concentration within the fluid, which will fall within each layer due to the adsorptive removal by previous layers. Thus the pore radius will decrease at a slower rate in each successive layer, and so we expect that a constricting filter set-up will offer the filtration configuration that clogs for the largest throughput.

This hypothesis is supported by considering the decline in mean pore radius with throughput in each layer (Fig. 5). For taper angles below the optimal value the first layer captures a much larger proportion of contaminant than the pores in the deeper layers (Fig. 5a and b). Conversely, when the taper angle is larger than the optimal value the final layer clogs before the other layers have trapped as much material as possible (Fig. 5d). At the optimal taper angle, the radius of each layer is approximately constant at the point of blocking (Fig. 5c).

We note that small changes in taper angle can generate significant differences in the final throughput. For example, a difference of less than 2° can lead to twice the final throughput before blocking. However, although such differences appear minimal, it is important to note that small taper angles translate to significant

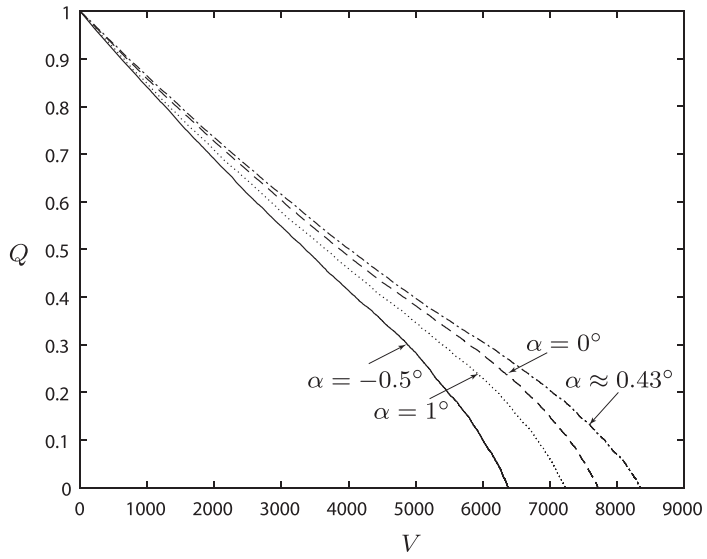

Fig. 3. Flux Q versus throughput V for a non-connected ($\gamma = 0$) five-layer filter ($N=5$) with particle size $a=0.5$, adhesivity $p_a=0.1$, filter depth $h=20$ and taper angle $\alpha = -0.5°$ (solid), $0°$ (dashed), $\alpha^* \approx 0.43°$ (dot-dashed), $1°$ (dotted) illustrating the increase and then decrease in final throughput V^* with increasing taper angle.

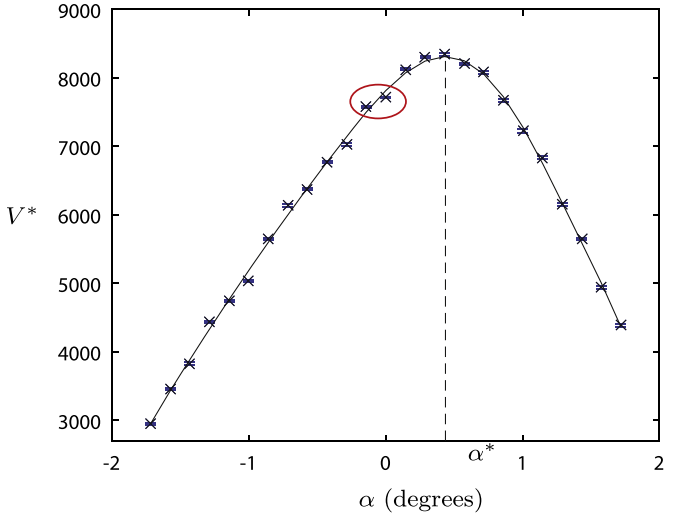

Fig. 4. Final throughput V^* versus taper angle α for a non-connected ($\gamma = 0$) five-layer filter ($N=5$) with particle size $a=0.5$, adhesivity $p_a=0.1$, and total filter depth $h=20$. The crosses show the data points and variance from the mean generated by the simulations, and the black curve is a polynomial fit with optimum at $\alpha^* \approx 0.43°$. The two circled data points correspond to $\alpha = 0°$ and $-0.14°$.

pore variations in our filter. For example, a filter with a taper angle of $2°$ corresponds to minimum and maximum radii of approximately 0.65 and 1.35 in the filter layers, respectively.

In addition to the improved total throughput offered by a constricting filter, such a set-up has the added advantage of allowing sequential filtering of a polydisperse feed, which would also assist in ensuring that the entire depth of a filter is utilized. While such a scenario is not studied here, the network model readily caters for such feed compositions.

5.2. The effect of particle size

While we were able to draw a continuous polynomial curve through the data in Fig. 4 to emphasize a continuous dependence of total throughput on taper angle, on closer inspection the data actually varies discontinuously with taper angle. This is especially apparent for the two data points at $\alpha = 0°$ and $\alpha = -0.14°$, for which the final throughput is seen to be approximately equal in both cases. While we might be tempted to attribute this to stochasticities within the system, any such randomness would be smoothed out by averaging over multiple runs. In fact, the feature actually arises due to an inherent discrete nature of the system. Specifically, the total number of particles that may be admitted by a pore before it blocks varies discretely with pore radius, governed by Eq. (15). Thus, as the taper angle varies, the number of particles that may be accepted by each individual layer will vary in a discrete manner (decreasing for layers whose pore radii are decreasing and increasing for layers whose pore radii are increasing). In particular, the total number of particles that can be accepted by the entire filter is given by

$$\mathcal{T} = \sum_{k=1}^{N} m \times n \times \text{Ceiling}\left(\frac{3(R_j(0)^2 - a^2)h}{4a^3}\right). \tag{16}$$

Crucially, the taper angle at which one additional particle can be accepted by each pore in a layer whose pore radii are increasing with increasing taper angle will not coincide with the point at which one less particle will be accepted by each pore in the layer whose pore radii are decreasing.

We plot the total number of particles that may be accepted by a filter per pore, $\mathcal{T}/(m \times n)$, in Fig. 6, which highlights the seemingly irregular behaviour, and hence the expected irregularities in the total throughput observed for a given filter. This discrete effect is particularly apparent when the particle size is comparable with the pore radii (cf. Figs. 4 and 7). In this case, 'windows' emerge within which changes in the taper angle have no effect on the total throughput. We are still able to approximate a curve through the data in this case, signifying that an optimum taper angle still exists for which the total throughput is maximized. However, in this case a range of taper angles now yields a similar total throughput close to the maximum. This feature may be useful in practice, where external considerations (such as design or financial factors on the taper angles that can be achieved) impose additional constraints on the system.

5.3. The optimum taper angle for small particles: a continuum approach

Having identified the behaviour when particles become comparable with the pore size, we now turn our attention to the

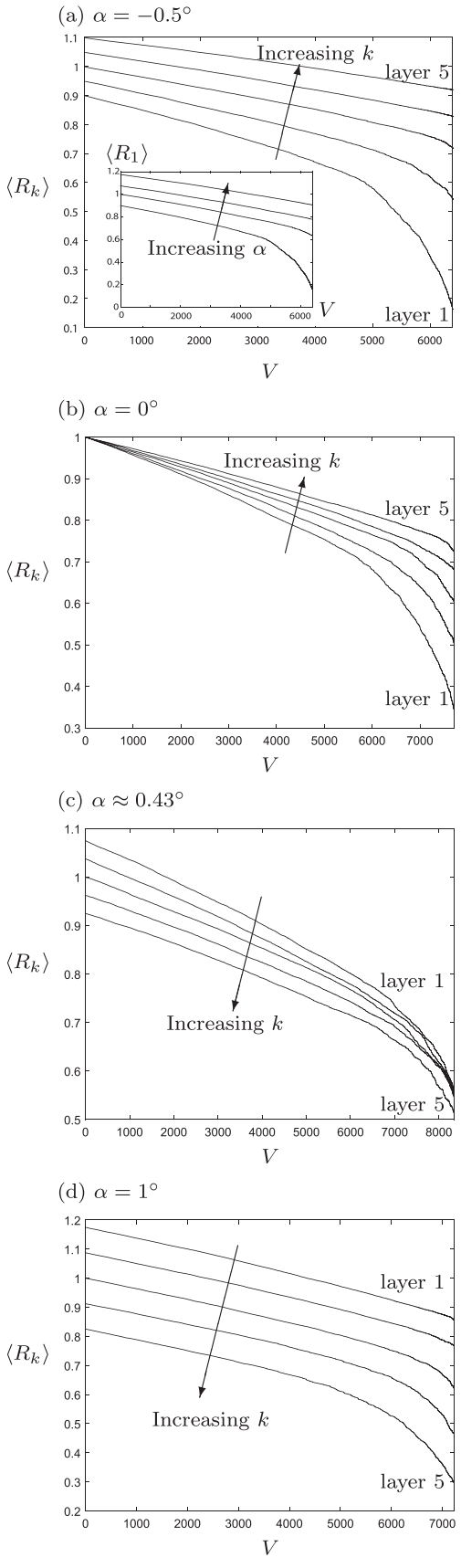

Fig. 5. Variation of mean pore radius $\langle R_k \rangle = \sum_{i=1}^{n} \sum_{j=1}^{m} r_k^{(i,j)}$ versus throughput V in a non-connected five-layer filter ($N=5$) for $1 \le k \le 5$ with taper angle (a) $\alpha = -0.5$, (b) $\alpha = 0$, (c) $\alpha = \alpha^* \approx 0.43$, (d) $\alpha = 1$ when filtering particles of size $a=0.5$ and adhesivity $p_a=0.1$. For the optimal taper angle the final radius of pores in each layer is approximately equal indicating optimal filter usage. (Note that the axes scaling differs in each case.) The inset in (a) compares the evolution of $\langle R_1 \rangle$ with throughput V for the four different taper angles shown in (a)–(d).

opposite limit, in which the particles are very small. In this case, filter clogging will be dominated by standard blocking, with complete blocking being an insignificant final feature in the QV signature. At each layer, a fraction p_a of particles will adhere to the pore wall and a fraction $(1 - p_a)$ will be transmitted. Thus, for our scaling choice such that one particle enters the membrane for each unit of throughput, a total of $(1 - p_a)^k V$ particles will be transmitted through to layer k with throughput V, of which a total $p_a(1 - p_a)^k V$ will adhere. The radius of a pore in layer k is therefore given by

$$r_k(t) = \sqrt{r_k(0)^2 - \frac{4a^3 N}{3h} p_a (1 - p_a)^{k-1} \frac{V}{mn}}, \tag{17}$$

where, for a uniformly tapered N-layer filter,

$$r_k(0) = 1 + \frac{h}{2N} \tan(\alpha) N + 1 - 2k. \tag{18}$$

The relationship (17) is indeed obeyed for sufficiently small particle sizes (Fig. 8), where the results for $a=0.2$ and the continuum description as $a \to 0$ are almost indistinguishable. However, we observe deviation from the predicted linear relationship between r_k^2 and throughput V as the particle sizes increases (Fig. 8).

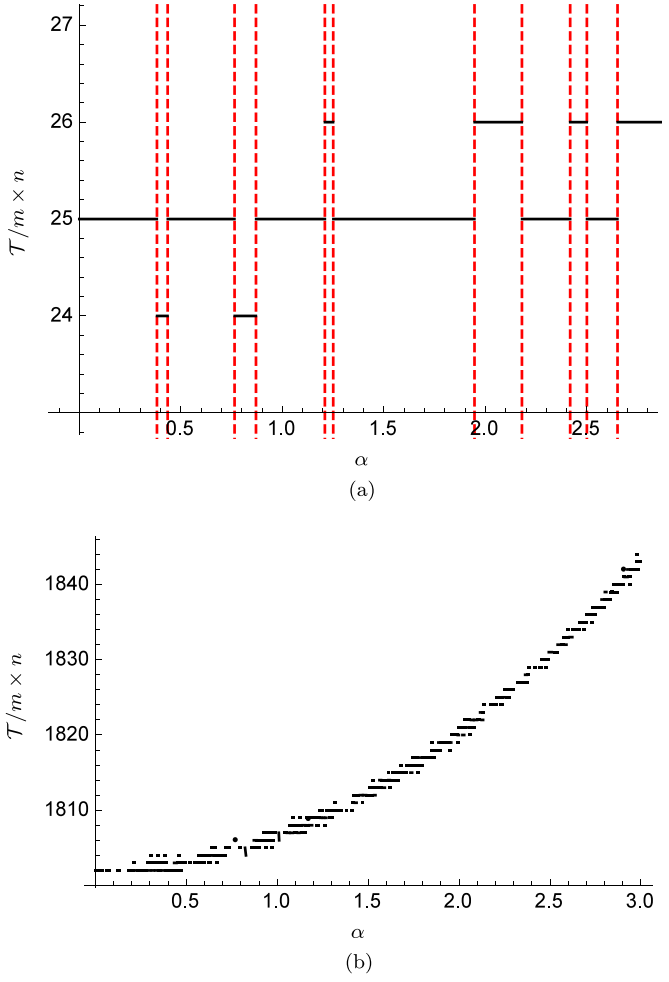

Fig. 6. Total number of particles of size (a) $a=0.7$ and (b) $a=0.2$ that can be accepted per pore ($\mathcal{T}/m \times n$) versus taper angle α for a non-connected ($\gamma = 0$) five layer filter $N=5$ with total membrane depth $h=20$. The (red) vertical dashed lines in (a) indicate the taper angles where a discrete change in the number of particles that may be accepted occurs. The approximately continuous dependence for smaller particles is apparent in (b). Note that the plots are symmetric about $\alpha = 0$.

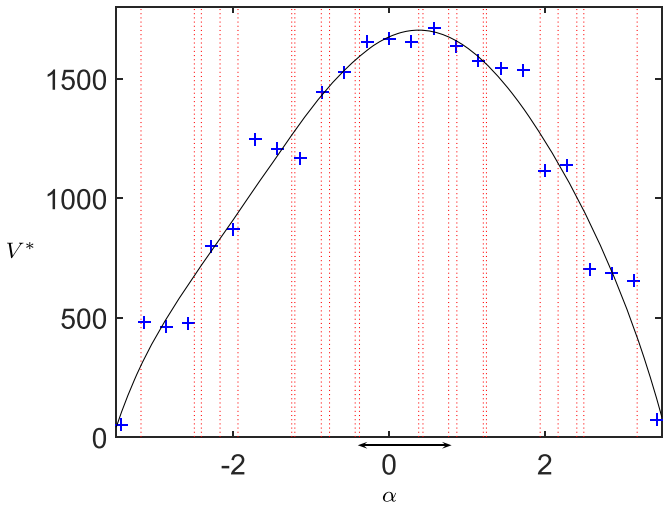

Fig. 7. Final throughput V^* versus taper angle α for a non-connected ($\gamma = 0$) five-layer filter ($N=5$) with particle size $a=0.7$, adhesivity $p_a=0.1$, and total filter depth $h=20$. The black curve is a polynomial fit to the data. The discrete variation in throughput with taper angle is much more apparent than when $a=0.5$ (Fig. 4) due to the discrete variations in the number of particles that may be accepted by the filter (Fig. 6). The (red) vertical dotted lines denote the taper angles that correspond to a change in the number of particles that can be accepted by the filter and separate the data into the expected discrete regions. The arrows show the region over which the throughput is approximately constant and maximal.

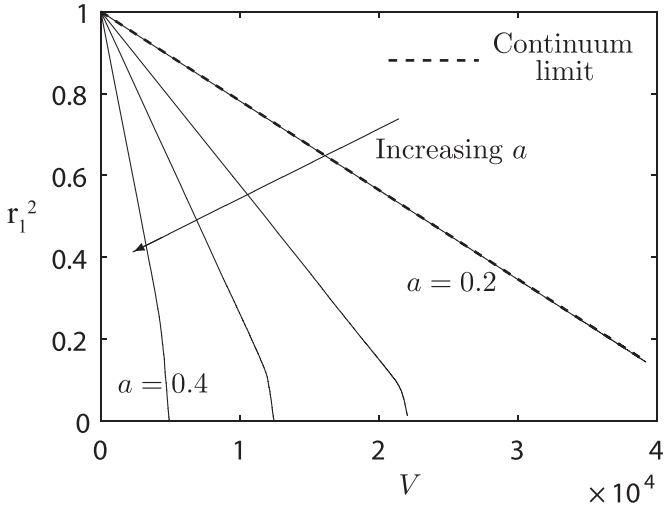

Fig. 8. Layer 1 pore radius squared $r_1(t)^2$ versus throughput V for a non-connected ($\gamma = 0$) five-layer filter ($N=5$) with filter depth $h=20$, angle $\alpha = 0$, adhesivity $p_a=0.4$ and particle size $a = 0.2, 0.25, 0.3, 0.4$. The continuum limit $a \to 0$ is shown by the dashed line, and is indistinguishable from the result for particle size $a=0.2$.

Having validated our continuum theory, we now use this to predict the taper angle that maximizes the throughput. Guided by Fig. 5, we observe that the throughput is maximized if the filter clogs when each of the filter layers has the same mean pore radius (see in particular Fig. 5c). Furthermore, we observe in Fig. 8 that as the particle size tends to zero, the mean pore radius at which blocking occurs will be zero. Thus, for a fixed taper angle, the throughput will be maximized when $r_1 = r_N = 0$ at blocking, which gives an optimal taper angle

$$\tan(\alpha^*) = \frac{2N}{(N-1)h}\frac{1-(1-k)^{(N-1)/2}}{1+(1-k)^{(N-1)/2}}. \qquad (19)$$

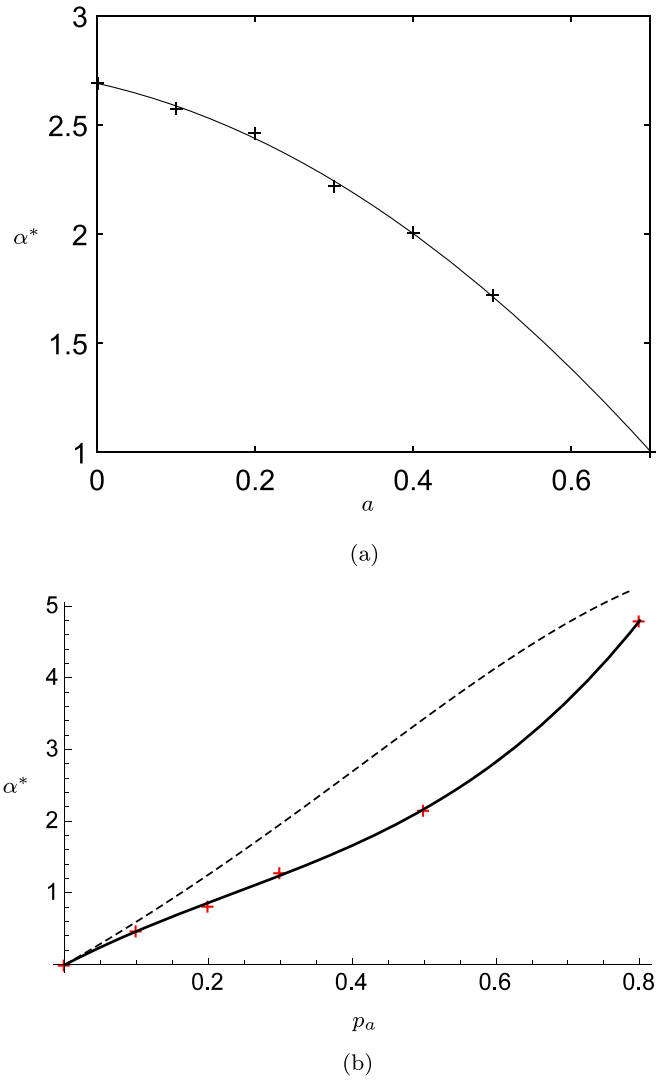

Fig. 9. Optimal taper angle α^* for a non-connected ($\gamma = 0$) five-layer filter ($N=5$) with total membrane depth $h=20$ versus: (a) particle size, a, when adhesivity $p_a=0.4$; (b) adhesivity, p_a for particle size $a=0.5$. The continuum limit for small particles, (19), is shown as a dashed curve in (b).

This prediction is compared with numerical results in the case of finite particle sizes in Fig. 9.

5.4. Parametric dependence of optimal taper angle

The results of the analysis in Sections 5.1 and 5.2 are unified in Fig. 9 in which the optimal taper angle is expressed for a given feed composition, characterized through particle size (Fig. 9a) and adhesivity with the membrane (Fig. 9b). The ability to map out the complete parameter landscape in this way reveals how the optimal taper angle increases with decreasing particle size and increasing adhesivity, and demonstrates how the network model is able to offer a strategy for selecting the appropriate membrane for a given filtration challenge.

6. Influence of pore interconnectivity

Having quantified the effect of taper angle for non-connected filters we now relax this condition to allow pore interconnectivity. As we might expect, allowing for interconnectivity increases the total volume of fluid that can be processed before the filter clogs.

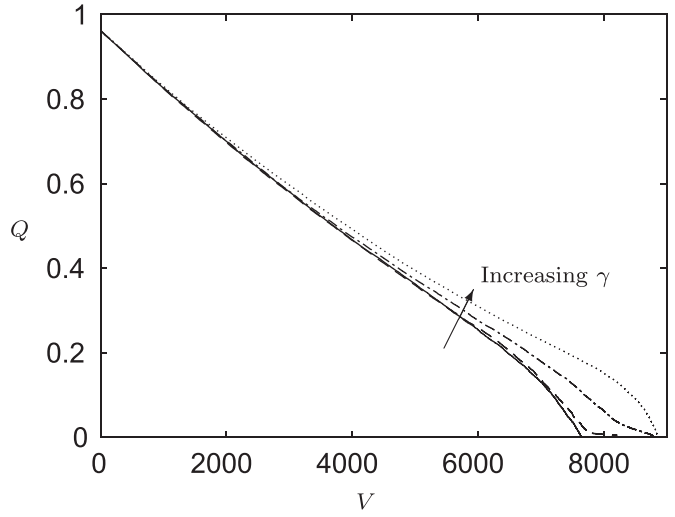

Fig. 10. Flux Q versus throughput V for a five-layer filter ($N=5$) with particle size $a=0.5$, adhesivity $p_a=0.1$, filter depth $h=20$, taper angle $\alpha=0$ and connectivity $\gamma=0$ (solid), 1×10^{-4} (dashed), 7×10^{-3} (dot-dashed), 0.02 (dotted). Only a small amount of connectivity is required to increase the throughput, which is achieved through a region of convexity in the QV signature. When γ is increased beyond approximately 7×10^{-3} the convex region begins to disappear while the final throughput V^* remains the same. The QV signature is unchanged by increases in connectivity beyond $\gamma\approx0.02$.

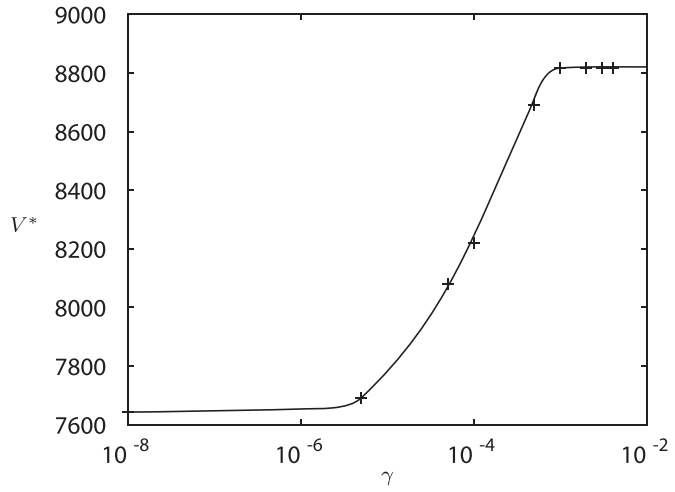

Fig. 11. Final throughput V^* versus pore interconnectivity γ for a five-layer filter ($N=5$) with particle size $a=0.5$, adhesivity $p_a=0.1$, total filter depth $h=20$, and taper angle $\alpha=0$. The crosses show the data points generated by the simulations and the black curve is a fit to the data.

The network model elucidates the route by which this is achieved, through the appearance of a convex tail region in the QV signature as γ increases (Fig. 10). When $\gamma\approx0.02$ the region of convexity begins to disappear, but the final throughput, V^*, remains approximately constant, enhanced by approximately 15% over the non-connected case. The subsequent QV signatures are then unchanged for pore connectivities that exceed $\gamma\approx0.02$. This informs us that, while allowing for pore interconnectivity in the filter is advantageous in improving the capacity of the filter before clogging, only a small amount of interconnectivity is needed to reap the benefits (Fig. 11). Thus, while it is worthwhile designing a filter with pore interconnectivity, this suggests that it may not be necessary to focus efforts on maximizing the interconnectivity within a filter. For a given γ, Eq. (14) provides a measure of the probability of a particle to progress directly into the pore below rather than traversing to a neighbouring pore before progressing

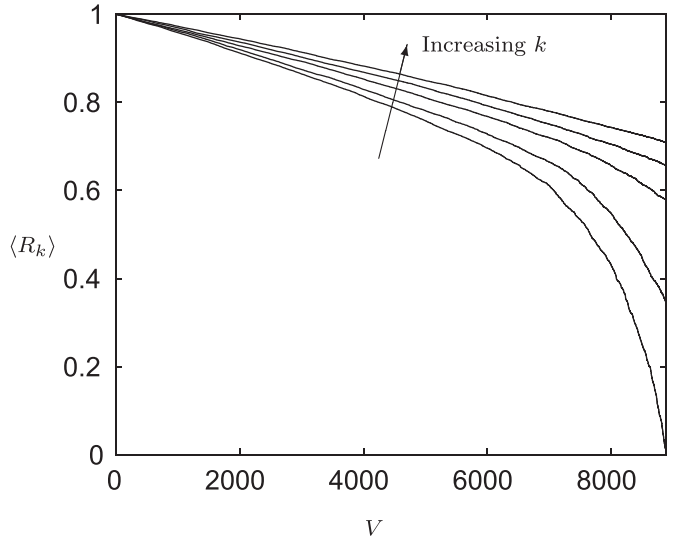

Fig. 12. Variation of mean pore radius $\langle R_k\rangle=\sum_{i=1}^{n}\sum_{j=1}^{m}r_k^{(i,j)}(t)$ versus time in a five-layer filter ($N=5$) for $1\le k\le5$ of depth $h=20$ with connectivity $\gamma=0.01$ and taper angle $\alpha=0$ when filtering particles of size $a=0.5$ and adhesivity $p_a=0.1$. The mean pore radius in layer 1 reaches zero when the final throughput is attained, indicating blocking of every pore.

to the next layer. For a polytetrafluoroethylene (PTFE) membrane, a typical value of κ is 0.3 [17]. For a five-layer membrane with total depth $h=20$ as examined here, this corresponds to a value of $\gamma\approx0.18$, which we observe to be within the region where pore connectivity is maximized in Fig. 11.

The reason behind the improved throughput can be identified by studying the constriction of the pore radii in each layer during filtration. Unlike in the case of a non-connected filter where the entire filter is able to clog without any individual layer being clogged (Fig. 5), a connected filter only blocks when *every* pore in one of the filter layers is blocked, so that the mean pore radius in this layer reaches zero. When the taper angle $\alpha=0$ it is layer 1 that blocks first, as seen in Fig. 12.

As the connectivity is increased, the throughput is found to vary more strongly with taper angle, so that the optimum taper angle is more prominent when the connectivity is suitably large while a range of taper angles that maximize throughput emerge as the connectivity is reduced (Fig. 13). This suggests that, while gains are made by increasing the throughput, design accuracy also becomes more important when maximizing the filter efficiency.

7. Influence of number of filter layers

Increasing the number of layers while holding the total filter thickness constant leads to a decrease in the final throughput (Fig. 14). This arises as a result of local layer blocking: the pore in a thinner layer will block sooner due to its reduced capacity for adsorbed particles. This therefore exposes a trade-off between the advantage offered by increasing the number of layers in selective sieving of particles and the decrease in throughput that is achieved when opting for thinner membrane layers. The final throughput attained depends approximately inversely on the number of layers, $V^*\propto N^{-1}$, and is unaffected by the taper angle or connectivity within the filter.

8. Influence of pore irregularity

In all of the modelling so far we have considered filters composed of layers with initially uniformly sized regularly arranged

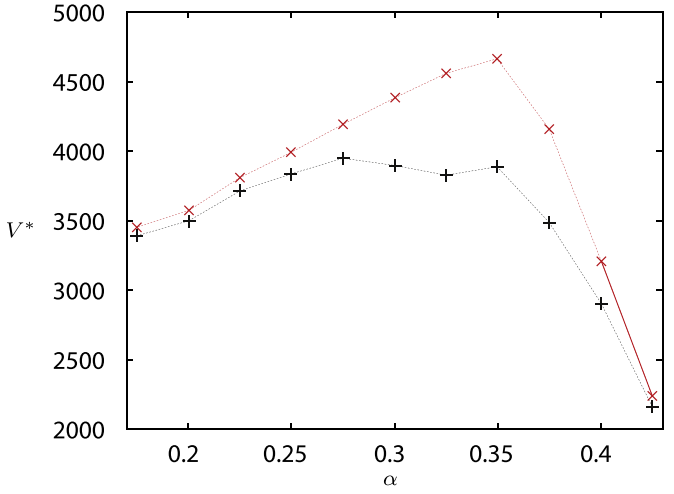

Fig. 13. Final throughput V^* versus taper angle α^* for a five-layer filter ($N=5$) with total membrane depth $h=20$ when filtering particles of size $a=0.5$ and adhesivity $p_a=0.4$. The black crosses (+) correspond to a filter with zero connectivity and the red crosses (×) corresponds to a filter with connectivity $\gamma = 0.01$. The connected and unconnected filters behave similarly away from the maximum but a more prominent and localized maximum exists when the filter has connectivity. (For interpretation of the references to colour in this figure caption, the reader is referred to the web version of this paper.)

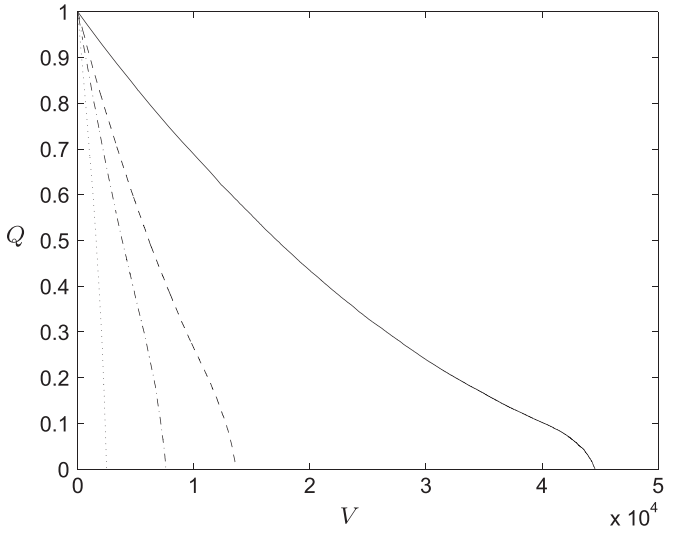

Fig. 14. Flux Q versus throughput V for a non-connected ($\gamma = 0$) filter with $N=1$ (solid), 3 (dashed) 5 (dot-dashed) and 11 (dotted) layers, of constant total filter thickness $h=20$ when filtering particles of size $a=0.5$ and adhesivity $p_a=0.1$.

pores, allowing only the pore radius between layers to differ, as exhibited, for example, by a track-etched membrane. However, in practice, filters can be composed of pores that are irregular in their size, position and number on each layer. In this final section we consider a generalized model that allows for randomly placed pores on each surface, whose size may differ across any single layer, and whose total number may vary from layer to layer. We retain the previously discussed network structure by assuming that each pore is connected to the five nearest neighbouring pores in the subsequent layer. The favourability of selecting pores that are closer in the layer below is accounted for by generalizing the hydraulic conductivity model proposed in Section 3 so that resistances scale linearly with the distance between a pore and a neighbour in the layer beneath. As before, we balance the incoming and outgoing fluxes through each junction to compute the

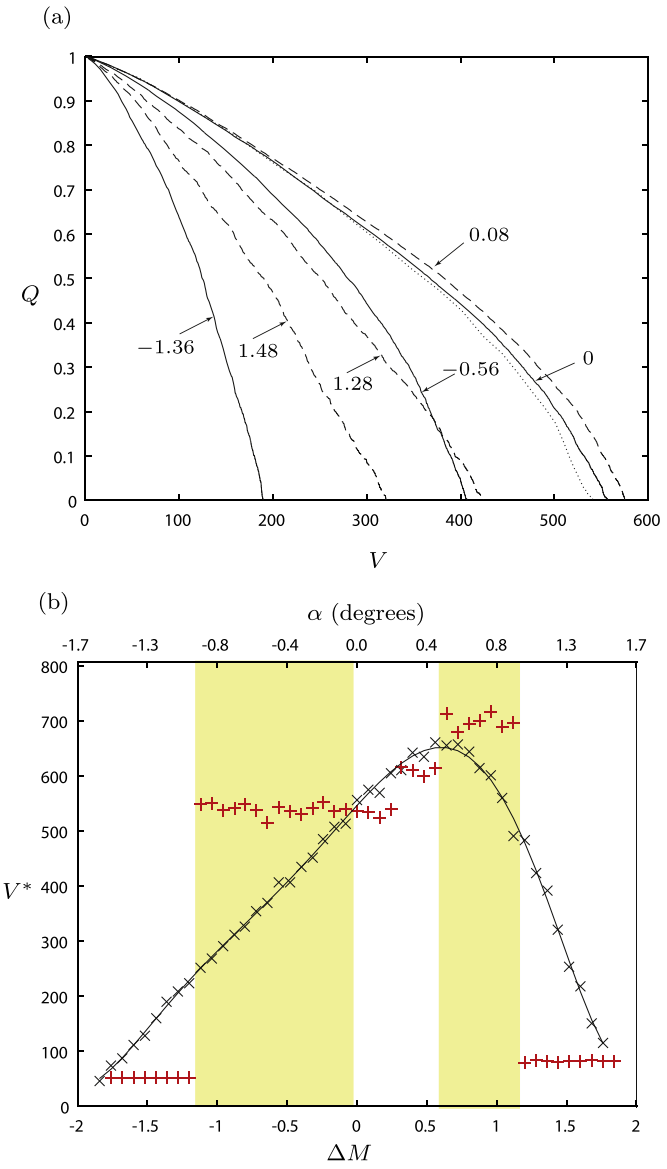

Fig. 15. (a) Flux Q versus throughput V for a random array fully connected ($\gamma = 1$) five-layer filter ($N=5$) with mean number of pores $\langle M \rangle = 50$, particle size $a=0.9$, adhesivity $p_a=0.1$, and total filter depth $h=20$. The results are averaged over 40 simulations of independent random arrays. The number of pores in each layer varies linearly with depth, with the difference from the mean between the top and bottom layers being $\Delta M = -1.36, -0.56, 0$ (solid) and $\Delta M = 0.08, 1.28, 1.44$ (dashed). Numbers on the graph indicate the corresponding values of ΔM. The throughput is maximal for a positive choice in ΔM, corresponding to a set-up in which the number of pores decreases with depth. The equivalent fully connected model for a periodic array of pores is shown by the dotted line, which is in agreement with the scenario where each layer has the same number of pores but arranged in a random array. (b) Total throughput V^* versus difference in pore number ΔM (black crosses ×) and versus taper angle α (red crosses +). The shaded/unshaded regions show the range for which a greater throughput is achieved by varying the pore size/pore number on each layer. The axes are aligned such that the corresponding variation in pore area achieved by either varying pore number or pore size is the same in each case. A polynomial curve of best fit is also shown for the data expressing the variation in throughput with ΔM. (For interpretation of the references to colour in this figure caption, the reader is referred to the web version of this paper.)

pressure at each end of the pore. Particles can still traverse side to side across the structure (depending on the magnitude of the fluxes) before entering a pore in the layer beneath.

We consider filters where the number of pores in each successive layer alters by a constant amount, and we characterize the variations in the number of pores between each layer by

$$\Delta M = \frac{M_1 - M_N}{\langle M \rangle}, \tag{20}$$

where M_i is the number of pores in layer i and

$$\langle M \rangle = \frac{1}{N}\sum_{i=1}^{N} M_i \tag{21}$$

is the mean number of pores in each layer of the filter.

We explore the effect of varying the porosity with depth but now achieve this by changing the pore density while holding the initial pore size fixed. As observed for variations in taper angle, the throughput is maximized when the porosity of each successive layer decreases (Fig. 15a dotted curve). A reassuring result is that the typical *QV* signature when we average over a series of 40 different random arrays amounts to a near identical *QV* signature to that of a regular array of pores arranged on the same pore area (Fig. 15a dotted curve). This validates our assumption that our regular-array model corresponds to the average behaviour of a series of many filters with the same number of randomly arranged pores.

As we vary the porosity gradient by changing the number of pores in each successive layer we find that the throughput is maximized for a multilayer configuration in which the porosity decreases with depth (Fig. 15b). This highlights a clear analogue with the set-up when we vary the porosity by changing the pore size in each layer for a filter composed of a periodic array (Figs. 4 and 7). However, we also find that, for two filters with equal porosity gradient, the characteristic behaviour of the filter differs significantly depending on whether we choose to grade porosity by varying the number of pores on each layer or by varying the pore size. In particular we find that by keeping the pore size fixed we no longer observe the discrete jumps in throughput that arise when the pore size and obstructing particle become comparable in size (as shown in Fig. 7). This leads to regimes in which the throughput for a given porosity gradient is larger when we change the pore size (shaded regions in Fig. 15b) and others where the largest throughput is achieved by changing the number of pores (unshaded regions in Fig. 15b). This effect would be reduced as the particle size decreases and the effect of changing the pore size becomes more continuous, as seen in Figs. 4 and 7. It is clear that if we have the manufacturing flexibility to change both the pore size and number density then its throughput can be significantly improved.

9. Conclusions

The improvements in filtration offered by multilayer filters are well-known experimentally, for example in allowing for selective sieving. However, a systematic study that examines the underlying mechanisms that lead to this sequential particle removal, and thus the optimal design requirements for such a filter, was lacking. We have developed a network model that allows for extensive and time-efficient parameter sweeps to determine the optimal filter structure for a given challenge feed and thus tackle this question. The model characterizes the filter (via taper angle, number of filter layers, and layer connectivity) and the feed composition (through the size of the particles and their adhesivity to the membrane). Both standard and complete blocking are catered for by the model in a systematic manner.

The existence of an optimal taper angle was found that corresponds to a filter whose mean pore radius decreases with depth (Fig. 5). For smaller taper angles than this the upper layer of the filter blocks before the lower layers have trapped comparable amounts of material; for larger taper angles the bottom layer of the filter blocks before the upper layers. When either the size of the particles or their adhesivity to the filter increases, the optimal taper angle increases, and we are able to map this systematically in parameter space (Fig. 5).

Designing a filter that permits connectivity between pores offers a significant advantage over non-connected filters, but we have shown that only a small amount of connectivity is needed to provide these gains. This suggests that additional effort in improving pore connectivity may not be worth the extra efforts. The total throughput that can be achieved by the filter was shown to be approximately inversely proportional to the number of layers in the filter, as a result of local blocking in the individual layers. This offers a trade-off between the merits of multilayer filters, such as their selective sieving properties, and the reduced throughput that they offer per unit membrane depth.

We concluded by presenting a generalized model that allows for a more physically realistic random array of pores on each filter layer in which each pore in a layer is connected to the five neighbouring pores in the subsequent layer. We showed that the periodic-array model provides a prediction for the average behaviour of such a random filter, but that the ability to alter the porosity of each layer by changing both the pore density and pore size provides an additional level of flexibility that allows us to maximize the throughput and thus efficiency of a given porosity-graded filter.

The results we present in this paper offer a strategy for the design of a multilayer filter to maximize their longevity and filtration efficiency. The comprehensive network model is easily able to simulate a multitude of filtration scenarios, and provides a framework for simple addition to accommodate more complex and specific filtration situations. A generalization of the model to account for blocking in the pore connections, polydisperse feed solutions, and a comprehensive analysis of the parameter space for random pore distributions and sizes are areas that are likely to offer further stimulating results to the membrane community.

Acknowledgements

IMG gratefully acknowledges support from the Royal Society through a University Research Fellowship.

References

[1] C.J.M. Van Rijn, Membrane filter and a method of manufacturing the same as well as a membrane, US Patent 5,753,014, 19 May 1998.
[2] K.H. Wollinsky, M.W.K. Saefkow, Filter for liquor filtration, US Patent 5,462,667, 31 October 1995.
[3] E. Koch, Multi-layer filter, US Patent 4,483,771, 20 November 1984.
[4] A.J. Burggraaf, K. Keizer, Synthesis of inorganic membranes, in: Inorganic Membranes Synthesis, Characteristics and Applications, Springer, Netherlands, 1991, pp. 10–63.
[5] S. Barg, D. Koch, G. Grathwohl, Processing and properties of graded ceramic filters, J. Am. Ceram. Soc. 92 (12) (2009) 2854–2860.
[6] L.E. Anderson, Filter element and method of making the same, US Patent 2,539,768, 30 January 1951.
[7] D. Dickerson, M. Monnin, G. Rickle, M. Borer, J. Stuart, Y. Velu, W. Haberkamp, J. Graber, Gradient density depth filtration system, US Patent Application 11/140,801, 31 May 2005.
[8] I. Vida-Simiti, N. Jumate, V. Moldovan, G. Thalmaier, N. Sechel, Characterization of gradual porous ceramic structures obtained by powder sedimentation, J. Mater. Sci. Technol. 28 (4) (2012) 362–366.
[9] S. Datta, S. Redner, Gradient clogging in depth filtration, Phys. Rev. E 58 (2) (1998) R1203.
[10] H. Chen, W.-S. Hung, C.-H. Lo, S.-H. Huang, M.-L. Cheng, G. Liu, K.-R. Lee, J.-Y. Lai, Y.-M. Sun, C.-C. Hu, R. Suzuki, T. Ohdaira, N. Oshima, Y.C. Jean, Free-volume depth profile of polymeric membranes studied by positron annihilation spectroscopy: layer structure from interfacial polymerization, Macromolecules 40 (21) (2007) 7542–7557.
[11] Y.C. Jean, J.D. Van Horn, W.-S. Hung, K.-R. Lee, Perspective of positron annihilation spectroscopy in polymers, Macromolecules 46 (18) (2013) 7133–7145.

[12] M. Rahimi, S.S. Madaeni, M. Abolhasani, A.A. Alsairafi, CFD and experimental studies of fouling of a microfiltration membrane, Chem. Eng. Process.: Process Intensif. 48 (9) (2009) 1405–1413.
[13] M.P. Dalwadi, I.M. Griffiths, M. Bruna, Understanding how porosity gradients can make a better filter using homogenization theory, Proc. R. Soc. A 471 (2015) 201504644.
[14] I.M. Griffiths, A. Kumar, P.S. Stewart, A combined network model for membrane fouling, J. Colloid Interface Sci. 432 (2014) 10–18.
[15] B.F. Ruth, Studies in filtration III. Derivation of general filtration equations, Ind. Eng. Chem. 27 (6) (1935) 708–723.
[16] H. Ockendon, J.R. Ockendon, Viscous Flow, vol. 13, Cambridge University Press, Cambridge, 1995.
[17] C.-C. Ho, A.L. Zydney, Measurement of membrane pore interconnectivity, J. Membr. Sci. 170 (1) (2000) 101–112.